https://doi.org/10.5194/egusphere-2026-4717
Preprint. Discussion started: 21 August 2026

An integrated diagnostic framework for evaluating Brewer–Dobson circulation transport efficiency in a warming climate using CMIP6 and Aura MLS

Jackson Hian-Wui Chang[1,2,*], Ahmad Fairudz bin Jamaluddin[3], Sharifah Faridah binti Syed Mahbar[3], Yong Jie Wong[4], Maggie Chel-Gee Ooi[5], Juneng Liew[6], Fuei Pien Chee[7], Jedol Dayou[8,9], Justin Sentian[7], Raul R. Cordero[10], Neng-Huei Lin[2]

[1]Preparatory Center for Science and Technology, University Malaysia Sabah (UMS), Jalan UMS, 88400, Kota Kinabalu, Sabah, Malaysia
[2]Department of Atmospheric Sciences, National Central University (NCU), Taoyuan, 32001, Taiwan
[3]National Climate Centre, Malaysian Meteorological Department, Petaling Jaya, Selangor, Malaysia
[4]Department of Bioenvironmental Design, Faculty of Bioenvironmental Sciences, Kyoto University of Advanced Science, Kyoto, 606-8501, Japan
[5]Centre of Tropical Climate Change System, Institute of Climate Change, National University of Malaysia (UKM), Bangi, 43600, Malaysia
[6]Department of Earth Sciences and Environment, Faculty of Sciences and Technology, National University of Malaysia (UKM), Bangi, 43600, Malaysia
[7]Faculty of Science and Technology, University Malaysia Sabah (UMS), Jalan UMS, 88400, Kota Kinabalu, Sabah, Malaysia
[8]Energy, Vibration and Sound Research Laboratory (e-VIBS), Faculty of Science and Technology, University Malaysia Sabah (UMS), Jalan UMS, 88400, Kota Kinabalu, Sabah, Malaysia
[9]Centre for Instrumentation and Science Services (CISS), University Malaysia Sabah (UMS), Jalan UMS, 88400, Kota Kinabalu, Sabah, Malaysia
[10]Department of Physics, Universidad de Santiago de Chile, Santiago, CA, USA

**Correspondence to*: Jackson Hian-Wui Chang (jacksonchw@ums.edu.my)

Abstract. The Brewer–Dobson circulation plays a fundamental role in regulating the transport of trace gases, water vapor, and ozone throughout the stratosphere, yet quantifying changes in its transport efficiency under greenhouse warming remains challenging because no single diagnostic fully characterizes large-scale transport. Here, we develop an integrated diagnostic framework that combines Coupled Model Intercomparison Project Phase 6 climate simulations with Aura Microwave Limb Sounder satellite observations to evaluate changes in Brewer–Dobson circulation transport efficiency. The framework integrates mean age of air, Transformed Eulerian Mean diagnostics, Eliassen–Palm flux divergence, and tracer propagation derived from daily water vapor observations. Multi-model simulations show widespread reductions in mean age of air from the pre-industrial period through future SSP370 projections, indicating progressively younger stratospheric air and enhanced large-scale transport. Dynamical diagnostics reveal strengthened wave-driven residual circulation, with the largest response occurring in the lower stratosphere. Independent satellite observations show coherent tropical-to-extratropical tracer

https://doi.org/10.5194/egusphere-2026-4717
Preprint. Discussion started: 21 August 2026

propagation, with the fastest transport occurring within the 400–500 K layer and substantially slower transport above 500 K. Sensitivity analyses using monthly observations and alternative lag thresholds reproduce the same vertical transport hierarchy, demonstrating the robustness of the results. Together, the complementary model and observational diagnostics show that greenhouse-driven changes in the Brewer–Dobson circulation are expressed primarily through enhanced lower-stratospheric transport efficiency rather than major changes in circulation structure. The proposed framework provides a physically consistent approach for evaluating future stratospheric transport and an observational benchmark for assessing climate-model projections.

Keywords: Brewer–Dobson circulation; stratospheric transport; age of air; Aura MLS; CMIP6; water vapor tracer diagnostics

1 Introduction

The Brewer–Dobson circulation (BDC) is the dominant large-scale overturning circulation of the stratosphere and plays a central role in regulating the transport and redistribution of trace gases, aerosols, ozone, and water vapor (Butchart, 2014). The circulation is characterized by tropical upwelling (Salby and Callaghan, 2006), poleward transport in the stratosphere (Poshyvailo-Strube et al., 2022), and extratropical downwelling at middle and high latitudes. Through these processes, the BDC strongly influences stratospheric composition, radiative balance, ozone recovery, and coupling between the troposphere and stratosphere (Poshyvailo-Strube et al., 2022). Variations in BDC transport therefore have important implications for atmospheric chemistry, climate feedbacks, and the long-term evolution of the middle atmosphere (Hufnagl et al., 2023).

A substantial body of modeling evidence suggests that greenhouse-gas forcing is associated with an acceleration of the Brewer–Dobson circulation. Climate-model simulations from CMIP5 and CMIP6 consistently indicate reductions in the mean age of stratospheric air (AoA), implying shorter transport timescales and more rapid meridional redistribution of tracers under a warming climate (Šácha et al., 2019) (Garcia and Randel, 2008). Previous studies have additionally linked these changes to enhanced wave–mean flow interaction and stronger residual circulation transport driven by increasing planetary-wave forcing in the lower stratosphere (Gerber, 2012) (Mclandress and Shepherd, 2009). Although the overall geometry of the BDC appears relatively stable across climate projections, numerous studies suggest that transport efficiency within the lower stratosphere may increase substantially during the 21st century (Rivoire et al., 2023).

Despite broad model agreement regarding accelerated transport, important uncertainties remain concerning the vertical structure and dynamical expression of these changes. In particular, it remains unclear whether greenhouse-forced BDC acceleration primarily reflects stronger overturning circulation, enhanced tracer redistribution efficiency, changes in wave-driven mixing, or a combination of these processes. Mean residual circulation diagnostics alone may not fully characterize

https://doi.org/10.5194/egusphere-2026-4717
Preprint. Discussion started: 21 August 2026

large-scale transport because tracer propagation depends not only on vertical advection but also on horizontal mixing, recirculation, and wave-driven transport variability (Šácha et al., 2024; Zajíček et al., 2024). Consequently, additional observational constraints are required to better understand how transport efficiency evolves across different regions of the stratosphere.

Long-lived tracers provide an important observational framework for diagnosing large-scale stratospheric transport. Water vapor (H_2O) is particularly useful because its variability reflects both tropical source processes and subsequent meridional redistribution by the Brewer–Dobson circulation (Randel et al., 2024). Previous observational studies have demonstrated that tracer anomalies associated with volcanic eruptions, tropical moistening events, and seasonal variability can reveal coherent transport pathways extending from the tropics toward the extratropics (Chang et al., 2025; Flury et al., 2013). Satellite observations from the Aura Microwave Limb Sounder (MLS) additionally provide long-term, vertically resolved measurements of stratospheric H_2O suitable for examining large-scale transport variability across multiple latitude bands and potential temperature layers (Clark et al., 1998; Kawatani et al., 2014).

Recent advances in tracer-based diagnostics have further enabled the use of lag-correlation frameworks to estimate effective transport timescales and propagation pathways within the stratosphere (Hall and Waugh, 1997; Hoor et al., 2010). In particular, tracer propagation approaches following (Flury et al., 2013) provide a useful framework for relating time-delayed correlations between tropical and extratropical anomalies to effective transport efficiency. However, most previous large-scale observational transport studies have focused on monthly or seasonal diagnostics, which can obscure the continuous temporal evolution of tracer propagation and limit characterization of vertically varying transport structure (Tweedy et al., 2017). Daily anomaly analyses may provide improved constraints on the timing and evolution of large-scale transport pathways, although they additionally require careful treatment of persistence-related covariance and short-timescale autocorrelation.

The Brewer–Dobson circulation may be characterized using several complementary diagnostics that describe different aspects of stratospheric transport. Mean age of air integrates the cumulative transport timescale experienced by air parcels, whereas residual circulation diagnostics describe the large-scale overturning responsible for mass transport (Gerber, 2012). Eliassen–Palm flux divergence characterizes the dynamical forcing driving the circulation (Baikhadzhaev et al., 2025) while tracer propagation diagnostics quantify the efficiency with which tracer anomalies are redistributed throughout the stratosphere (Poshyvailo-Strube et al., 2022). Because these diagnostics describe different but complementary aspects of transport, combining them provides a more complete framework for interpreting greenhouse-forced changes in stratospheric circulation than any individual diagnostic alone.

https://doi.org/10.5194/egusphere-2026-4717
Preprint. Discussion started: 21 August 2026

In this study, we develop an integrated framework for diagnosing changes in Brewer–Dobson circulation transport efficiency by combining complementary dynamical and observational diagnostics. Rather than relying solely on traditional circulation metrics such as residual velocity or age of air, we combine CMIP6 age-of-air, Transformed Eulerian Mean diagnostics, wave-driven momentum forcing, and daily Aura MLS water-vapor tracer propagation to characterize how greenhouse forcing modifies large-scale stratospheric transport. This framework allows us to distinguish changes in transport efficiency from changes in the overall geometry of the circulation. We further provide an observational constraint on modeled transport changes by estimating effective tracer propagation timescales from daily MLS observations, thereby linking simulated circulation changes directly with observed tracer redistribution.

2. Data & Methods

2.1 Climate Model Simulations: CMIP6

We utilize CMIP6 models that produce Age of Stratospheric Air (AoA) and Transformed Eulerian Mean (TEM) data required for investigating the variability of Brewer-Dobson Circulation (BDC) strength, as outlined in Gerber & Manzini (2016). Detailed diagnostic descriptions are available in their paper (Gerber and Manzini, 2016). Tables 1 and 2 list the selected models driven by the historical and SSP370 scenarios, respectively, along with their variant labels, realms, and spatial and temporal resolutions. While the horizontal resolution varies among models, it generally ranges between 1° and 2° in latitude. To ensure statistical robustness, we include all available variant labels, as the standard setting (typically labeled i1p1f1) often lacks sufficient ensemble members to yield meaningful results (Bunzel and Schmidt, 2013). However, this approach requires significant computational resources, necessitating ensemble averaging to obtain reliable conclusions. For each model, we use all available runs with different initialization (i), physics (p), and forcing (f) settings.

We use AoA and TEM outputs to evaluate past climatology and trends in BDC patterns under both historical and SSP370 scenarios. Given the varying number of ensemble members across models (ranging from 1 to 25), we incorporate all available members for each simulation, averaging them when multiple runs are available to minimize the impact of internal variability on long-term trends. For AoA, a total of 39 (24) members from CMIP6 historical (SSP370) experiments are included in the multi-model ensemble, covering models such as CNRM-ESM2-1, MRI-ESM2-0, and UKESM1-0-LL. For TEM upward wind (wtem), a total of 61 (85) members from CMIP6 historical (SSP370) experiments are used, including models such as CanESM5, CanESM5-1, CanESM5-CanOE, CESM, CESM2-WACCM, CNRM-ESM2-1, HadGEM3-GC31-LL, HadGEM3-GC31-MM, MIROC6, and UKESM1-0-LL. For TEM stream function (psitem), only one ensemble member from the MIROC6 historical experiment is available.

To further explore decadal variations in BDC, we analyze TEM zonal wind tendency using CMIP6 simulations under the 1% per year CO_2 increase (1pctCO2) scenario (Garcia and Randel, 2008). This scenario provides a controlled framework to

https://doi.org/10.5194/egusphere-2026-4717
Preprint. Discussion started: 21 August 2026

assess the impact of increasing greenhouse gas (GHG) concentrations on stratospheric circulation and wave-mean flow interactions. We examine the zonal wind tendency components, including utendepfd (eddy-driven forcing), utendnogw (resolved wave forcing excluding orographic gravity waves), and utendogw (orographic gravity wave forcing), to determine their respective contributions to stratospheric momentum deposition (Table 3). To investigate altitude-dependent trends, we focus on key pressure levels associated with the shallow (100–30 hPa) and deep (30–1 hPa) branches of the BDC, as changes in momentum deposition at these levels provide insight into the evolving structure of the circulation .

Table 1. List of CMIP6 simulations driven by historical scenario with Mean Age of Stratospheric Air (meanage), Transformed Eulerian Mass (TEM) stream function (psitem) and upward velocity (wtem) used in the study. Number in bracket (n) in variant label represents the number of ensemble members available from the experiment.

Source ID	**Variant Label**	**Realm**	**Variable**	**Period**	**Spatial**	**Temporal**
CanESM5	ri1p2f1 (25)	Atmos	wtem	1850-2014	500 km	Monthly
CNRM-ESM2-1	ri1p1f2 (9)	Aerosol	meanage	1850-2014	250 km	Monthly
HadGEM3-GC31-LL	ri1p1f3 (5)	Atmos	wtem	1850-2014	100 km	Monthly
HadGEM3-GC31-MM	ri1p1f3 (2)	Atmos	wtem	1850-2012	100 km	Monthly
MIROC6	ri1p1f1 (1)	Atmos	wtem	1850-2014	250 km	Monthly
	ri1p1f1 (1)	Atmos	psitem	1850-2014	250 km	Daily
MRI-ESM2-0	ri1p1f1 (11)	Aerosol	meanage	1870-2014	500 km	Monthly
	ri1p1f1 (10)	Atmos	wtem	1850-2014	100 km	Monthly
UKESM1-0-LL	ri1p1f2 (16)	Aerosol	meanage	1850-2014	250 km	Monthly
	ri1p1f2 (15)	Atmos	wtem	1850-2014	250 km	Monthly
	ri1p1f3 (3)	Aerosol	meanage	1850-2014	250 km	Monthly
	ri1p1f3 (3)	Atmos	wtem	1850-2014	250 km	Monthly

Table 2. List of CMIP6 simulations driven by SSP370 scenario with Mean Age of Stratospheric Air (meanage), Transformed Eulerian Mass (TEM) upward velocity (wtem) diagnostic used in the study. Number in bracket (n) in variant label represents the number of ensemble members available from the experiment.

Source ID	**Variant Label**	**Realm**	**Variable**	**Period**	**Spatial**	**Temporal**
CanESM5	ri1p1f1 (15)	Atmos	wtem	2015-2100	500 km	Monthly
	ri1p2f1 (25)	Atmos	wtem	2015-2100	500 km	Monthly
CanESM5-1	ri1p1f1 (10)	Atmos	wtem	2015-2100	500 km	Monthly
	ri1p2f1 (10)	Atmos	wtem	2015-2100	500 km	Monthly
CanESM5-CanOE	ri1p2f1 (3)	Atmos	wtem	2015-2100	500 km	Monthly
CESM	ri1p1f1 (3)	Atmos	wtem	2015-2100	100 km	Monthly
CESM2-WACCM	ri1p1f1 (3)	Atmos	wtem	2015-2100	100 km	Monthly
CNRM-ESM2-1	ri1p1f2 (5)	Aerosol	meanage	2015-2100	250 km	Monthly
UKESM1-0-LL	ri1p1f2 (19)	Aerosol	meanage	2015-2100	250 km	Monthly
	ri1p1f2 (19)	Atmos	wtem	2015-2100	250 km	Monthly

https://doi.org/10.5194/egusphere-2026-4717
Preprint. Discussion started: 21 August 2026

Table 3. List of CMIP6 simulations driven by 1ptCO2 scenario with tendency of eastward wind due to TEM diagnostic used in the study. Number in bracket (n) in variant label represents the number of ensemble members available from the experiment.

Source ID	utendepfd	utendnogw	utendogw	utendvtem	utendwtem	Period	Spatial
CanESM5	r1p1f1 (2) r1p2f1 (3)	-	r1p1f1 (2) r1p2f1 (3)	r1p1f1 (2)* r1p2f1 (3)*	r1p1f1 (2)* r1p2f1 (3)*	1850-1999	500 km
HadGEM3-GC31-LL	r1p1f3 (4)	r1p1f3 (4)*	r1p1f3 (4)	-	-	1850-1999	100 km
HadGEM3-GC31-MM	r1p1f3 (1)	r1p1f3 (1)*	r1p1f3 (1)	-	-	1850-1999	100 km
MRI-ESM2-0	r1p1f1 (1) r2p1f1 (1)	r1p1f1 (1) r2p1f1 (1)	r1p1f1 (1) r2p1f1 (1)	r1p1f1 (1)*	r1p1f1 (1)*	1850-1999	100 km
UKESM1-0-LL	r1p1f2 (4)	r1p1f2 (4)*	r1p1f2 (4)	-	-	1850-1999	250 km

* Daily resolution; Total ensemble = 60 members

The historical simulations in CMIP6 generally span from 1850 to 2015, incorporating observed greenhouse gas emissions and other external forcings (e.g., f1, f2, f3). These simulations are used to analyze pre-industrial and past trends, with a focus on three key periods: 1850–1900 (pre-industrial), 1901–1974 (past trend), and 1975–2014 (recent trend). The pre-industrial period follows the IPCC definition (1850–1900), while the two past trend periods represent the industrial era before and after the 1987 Montreal Protocol. These temporal divisions are consistent with previous CMIP6 community studies (Smith and Forster, 2021; Zanis et al., 2020). The SSP370 scenario in CMIP6, which typically spans from 2015 to 2100, represents a medium-to-high emissions pathway where global GHG emissions continue rising throughout the 21st century. This scenario assumes moderate economic growth, high population growth, and limited advancements in energy efficiency and climate policies. It is used to analyze future trends, with a focus on two key periods: 2015–2055 (near-future) and 2056–2100 (far-future).

2.2 Aura MLS Stratospheric Water Vapor Diagnostics

Stratospheric water vapor variability was analyzed using observations from the Aura Microwave Limb Sounder (MLS) Level-3 zonal mean H_2O product in potential temperature coordinates (Carr et al., 1995; Kawatani et al., 2014). Daily zonal mean H_2O mixing ratios were obtained from the *H2O ThetaZM* group and processed over the 400–800 K isentropic layer to examine large-scale transport variability associated with the Brewer–Dobson circulation (BDC). The MLS H_2O fields were first converted from volume mixing ratio to parts per million by volume (ppmv) using

$$H_2O_{\mathrm{ppmv}} = H_2O \times 10^6$$

where H_2O denotes the original MLS volume mixing ratio. Unrealistic values and missing values were removed prior to analysis. The data were then interpolated and standardized into time x lev x lat dimensions for subsequent diagnostics. To emphasize large-scale transport variability and suppress short-timescale noise, a 31-point low-pass weighted smoothing filter equivalent to the NCL wgt_runave_n implementation was applied along the temporal dimension:

$$\tilde{x}(t) = \sum_{i=-15}^{15} w_i \, x(t+i)$$

https://doi.org/10.5194/egusphere-2026-4717
Preprint. Discussion started: 21 August 2026

where w_i represents the normalized low-pass filter weights and $x(t)$ denotes the original daily H_2O time series.

Daily climatological anomalies were subsequently computed relative to the day-of-year climatology following:

$$H_2O'(d,t) = H_2O(d,t) - \bar{H_2O}(d)$$

where $H_2O'(d,t)$ is the anomaly for day d and time t, and $\bar{H_2O}(d)$ denotes the climatological daily mean calculated over the full record after removing leap-day samples. The anomaly fields were averaged over six latitude bands representing the Southern Hemisphere (SH) and Northern Hemisphere (NH) tropics, midlatitudes, and polar regions: 30°S–0°, 60°S–30°S, 90°S–60°S, 0°–30°N, 30°N–60°N, and 60°N–90°N. Latitude-band means were computed using zonal averaging within each selected region.

Large-scale transport timescales were investigated using lag-correlation diagnostics between tropical and extratropical H_2O anomaly time series. Positive lag values indicate that tropical anomalies lead extratropical variability. The lag correlation coefficient was calculated as

$$r(\tau) = \frac{\sum_{t=1}^{N}[x(t)-\bar{x}]\,[y(t+\tau)-\bar{y}]}{\sqrt{\sum_{t=1}^{N}[x(t)-\bar{x}]^2\,\sum_{t=1}^{N}[y(t+\tau)-\bar{y}]^2}}$$

where $x(t)$ and $y(t)$ represent the tropical and extratropical anomaly time series, respectively, and τ denotes the lag time.

Lag diagnostics were first calculated using smoothed daily anomalies during the pre-eruption period (2004–2021) to isolate intrinsic BDC variability and minimize contamination from the large Hunga Tonga water vapor perturbation after 2022 (Coy et al., 2022; Yu et al., 2023). To further quantify transport efficiency, a second lag-correlation framework following the tracer propagation methodology of Flury et al. (2013) was applied using daily anomaly time series averaged within selected isentropic layers (400–500 K, 500–600 K, and 600–800 K). In this framework, tropical source anomalies were correlated with extratropical target anomalies over positive lag intervals to estimate tracer propagation timescales. The corresponding meridional transport speed was estimated as

$$c = \frac{D}{\tau}$$

where c is the effective tracer propagation speed, D is the great-circle meridional distance between latitude-band centers, and τ is the selected lag timescale. Because broad hemispheric coherence and autocorrelation can produce unrealistically short lag maxima, physically informed minimum lag thresholds were imposed prior to selecting the final propagation timescales. Thresholds of 45 days for tropical-to-midlatitude transport and 90 days for tropical-to-polar transport were applied to minimize spurious short-lag covariance (Flury et al., 2013; Hall and Waugh, 1997). Local correlation maxima satisfying these physical constraints were then identified using peak-detection analysis.

https://doi.org/10.5194/egusphere-2026-4717
Preprint. Discussion started: 21 August 2026

The two lag-correlation frameworks diagnose complementary aspects of BDC transport behavior. The first framework characterizes the temporal coherence and propagation structure of tropical-to-extratropical transport pathways using continuous lag-correlation functions, whereas the Flury-style framework converts physically constrained lag relationships into observational estimates of tracer transport efficiency and effective propagation speed. Together, these diagnostics provide an observational constraint on the vertical structure and variability of stratospheric transport associated with the Brewer–Dobson circulation.

2.3 Definition of Transport Efficiency

Transport efficiency is not directly measurable using a single atmospheric variable. Instead, it represents the effectiveness with which air masses and tracer anomalies are redistributed through the Brewer–Dobson circulation (BDC). Because different diagnostics describe different aspects of the transport process, no individual metric provides a complete characterization of transport efficiency (Butchart, 2014). In this study, transport efficiency is therefore inferred from multiple complementary diagnostics that collectively describe the physical processes governing large-scale stratospheric transport (Table 4).

The selected diagnostics represent different stages of the transport system. Mean age of air (AoA) provides an integrated measure of the cumulative transport timescale experienced by stratospheric air parcels, with younger air indicating more efficient large-scale transport. Transformed Eulerian Mean (TEM) diagnostics describe the resulting residual circulation and large-scale mass transport (Butchart, 2014; Gerber, 2012). Eliassen–Palm (EP) flux divergence characterizes the dynamical forcing associated with planetary-wave momentum deposition that drives the residual circulation. The MLS lag-correlation analysis characterizes the temporal coherence and propagation of observed tracer anomalies between tropical and extratropical regions, whereas the Flury-style tracer propagation framework converts physically constrained lag times into effective tracer propagation speeds (Hall and Waugh, 1997; Randel et al., 2024). Together, these diagnostics provide complementary evidence linking dynamical forcing, circulation response, integrated transport timescales, and observed tracer redistribution. Throughout this study, the term *transport efficiency* therefore refers to the collective interpretation derived from these multiple diagnostics rather than any single variable. The Results are organized according to this diagnostic hierarchy, progressing from integrated transport (AoA) to residual circulation (TEM), dynamical forcing (EP-flux), and finally observational tracer propagation (MLS).

Table 4. Complementary diagnostics used to characterize Brewer–Dobson circulation transport efficiency in this study.

Diagnostic level	**Variable**	**Physical quantity represented**

https://doi.org/10.5194/egusphere-2026-4717
Preprint. Discussion started: 21 August 2026

Integrated transport	AoA	Net transport timescale experienced by air parcels
Residual circulation	TEM w*, ψ*	Residual mass transport
Dynamical forcing	EP-flux divergence	Dynamical forcing that drives the circulation
Observed tracer propagation	MLS lag correlation	Satellite-observed redistribution of tracer anomalies
	MLS Flury-style propagation analysis	Satellite-observed effective tracer propagation speed

3. Results

3.1 Evidence of Accelerated Stratospheric Transport from Age of Air

The climatological structure of the age of stratospheric air (AoA) in CMIP6 reproduces the expected features of the Brewer–Dobson circulation (BDC), including tropical upwelling and poleward transport with pronounced hemispheric asymmetry. Across all historical periods, older air masses are concentrated in the polar stratosphere, particularly in the Southern Hemisphere during winter, consistent with weaker wave activity and more isolated polar vortex dynamics.

Despite similar spatial structures, substantial temporal changes emerge. The transition from the pre-industrial period (1850–1900) to the recent historical period (1975–2014) is characterized by a systematic reduction in AoA across all latitudes and seasons (Fig. 1). In particular, high-AoA isolines (>6 years), prominent in earlier periods, largely disappear in the recent period, accompanied by a marked weakening of the meridional gradient. This indicates a more rapid exchange between tropical and polar regions. Seasonal diagnostics further reveal that the accumulation of older air during transition seasons (MAM and SON) is substantially reduced in recent decades. While these seasons are traditionally associated with weaker circulation and longer residence times, the diminished persistence of older air suggests that enhanced transport efficiency now dominates over seasonal dynamical constraints.

Under the SSP370 scenario, this tendency intensifies (Fig. 2). In the far-future period (2056–2100), the upper stratosphere is dominated by substantially younger air masses (<4.4 years) across all seasons, indicating a continued acceleration of large-scale transport. Together, these results provide robust multi-model evidence that stratospheric transport has become progressively faster from the pre-industrial period to the end of the 21st century.

https://doi.org/10.5194/egusphere-2026-4717
Preprint. Discussion started: 21 August 2026

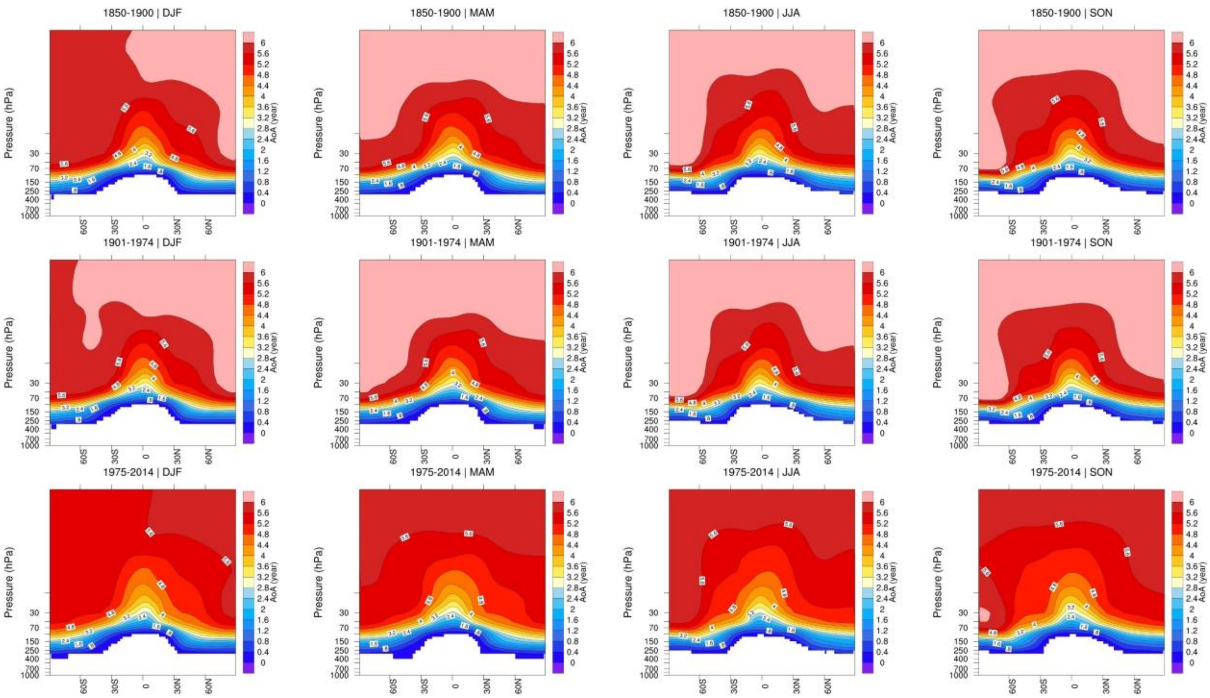

Figure 1. Latitude-pressure distribution of seasonally (DJF, MAM, JJA, SON) averaged AoA in pre-industry (1850-1900; top panel), past trend I (1901-1974; middle panel) and past trend II (1975-2014; bottom panel) from the CMIP6 multi-model ensemble simulation driven by historical scenario.

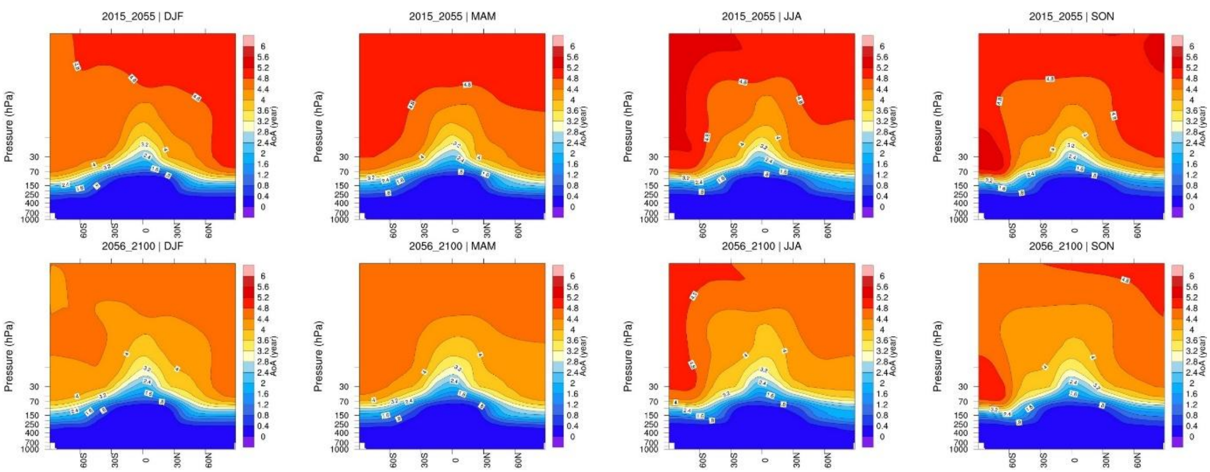

Figure 2. Latitude-pressure distribution of seasonally (DJF, MAM, JJA, SON) averaged AoA in near-future (2015-2055; top panel) and far-future (2056-2100; bottom panel) from the CMIP6 multi-model ensemble simulation driven by SSP370 scenario.

https://doi.org/10.5194/egusphere-2026-4717
Preprint. Discussion started: 21 August 2026

3.2 Dynamical Response of the Brewer–Dobson Circulation

The dynamical structure of the BDC is examined using the Transformed Eulerian Mean (TEM) vertical velocity (w*) and residual streamfunction (ψ*). The annually averaged TEM vertical velocity shows a persistent circulation pattern across all historical periods, with tropical upwelling and polar downwelling separated by a stable turnaround latitude near 30° in both hemispheres (Fig. 3). No significant latitudinal shift in this boundary is detected, indicating that the large-scale geometry of the BDC remains broadly unchanged.

However, changes in magnitude and variability are evident. While the mean tropical upwelling exhibits only modest increases in the historical period, enhanced vertical velocities are apparent in the upper stratosphere (>10 hPa) during the recent period, particularly during seasonal transition phases. This suggests that dynamical acceleration is not uniform but concentrated in specific regions and seasons. In contrast, future projections show a more pronounced intensification. Under SSP370, tropical upwelling strengthens significantly, with increased vertical velocities extending across a deeper layer of the stratosphere (Fig. 4). Concurrently, polar downwelling intensifies, reflecting mass conservation within a stronger overturning circulation. Notably, the turnaround latitude remains approximately stable across both historical and future periods, indicating that the large-scale geometry of the Brewer–Dobson circulation is largely preserved under greenhouse gas forcing.

Although residual streamfunction output is available only from MIROC6, this diagnostic provides an illustrative example of how changes in overturning circulation accompany the multi-model transport diagnostics (Fig. 5). The streamfunction analysis is therefore interpreted as supporting evidence rather than as an independent multi-model constraint. Positive trends in the Northern Hemisphere and negative trends in the Southern Hemisphere indicate enhanced poleward mass flux, particularly in the lower stratosphere. These changes are consistent with an intensification of the overturning circulation, even in the absence of large increases in mean vertical velocity. Taken together, the dynamical diagnostics indicate that while the spatial structure of the BDC remains stable, its intensity and variability increase over time, with stronger responses emerging under future forcing. These dynamical changes provide a basis for interpreting the reduction in AoA (Figs. 1–2), suggesting that enhanced transport efficiency is linked to changes in circulation strength and variability.

https://doi.org/10.5194/egusphere-2026-4717
Preprint. Discussion started: 21 August 2026

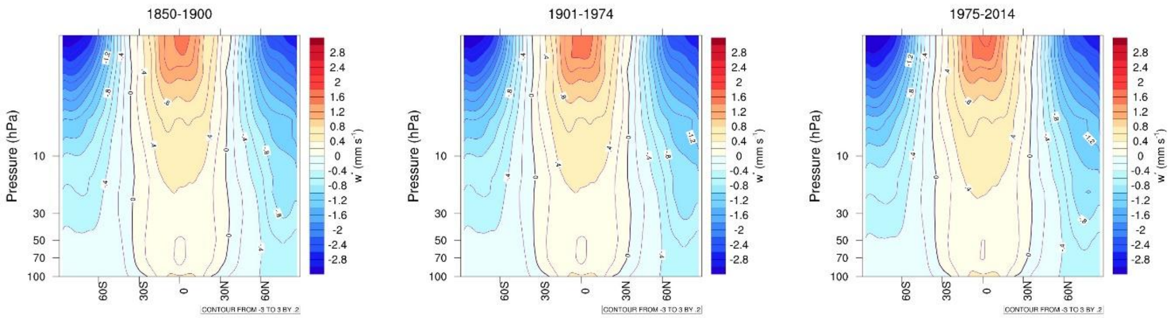

Figure 3. Latitude-pressure distribution of annually averaged Transformed Eulerian Mean (TEM) vertical wind speed (*w**) in pre-industry (1850-1900), past trend I (1901-1974) and past trend II (1975-2014) from the CMIP6 multi-model ensemble simulation driven by historical scenario. Black thick contours indicate the location of the turnaround latitudes.

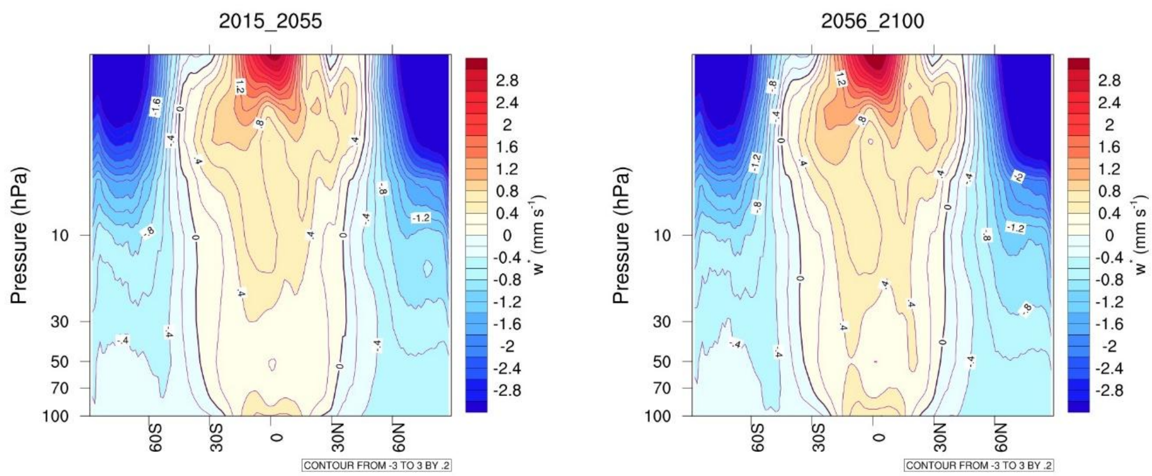

Figure 4. Latitude-pressure distribution of annually averaged TEM upward wind in near-future (2015-2055) and far-future (2056-2100) from the CMIP6 multi-model ensemble simulation driven by SSP370 scenario.

https://doi.org/10.5194/egusphere-2026-4717
Preprint. Discussion started: 21 August 2026

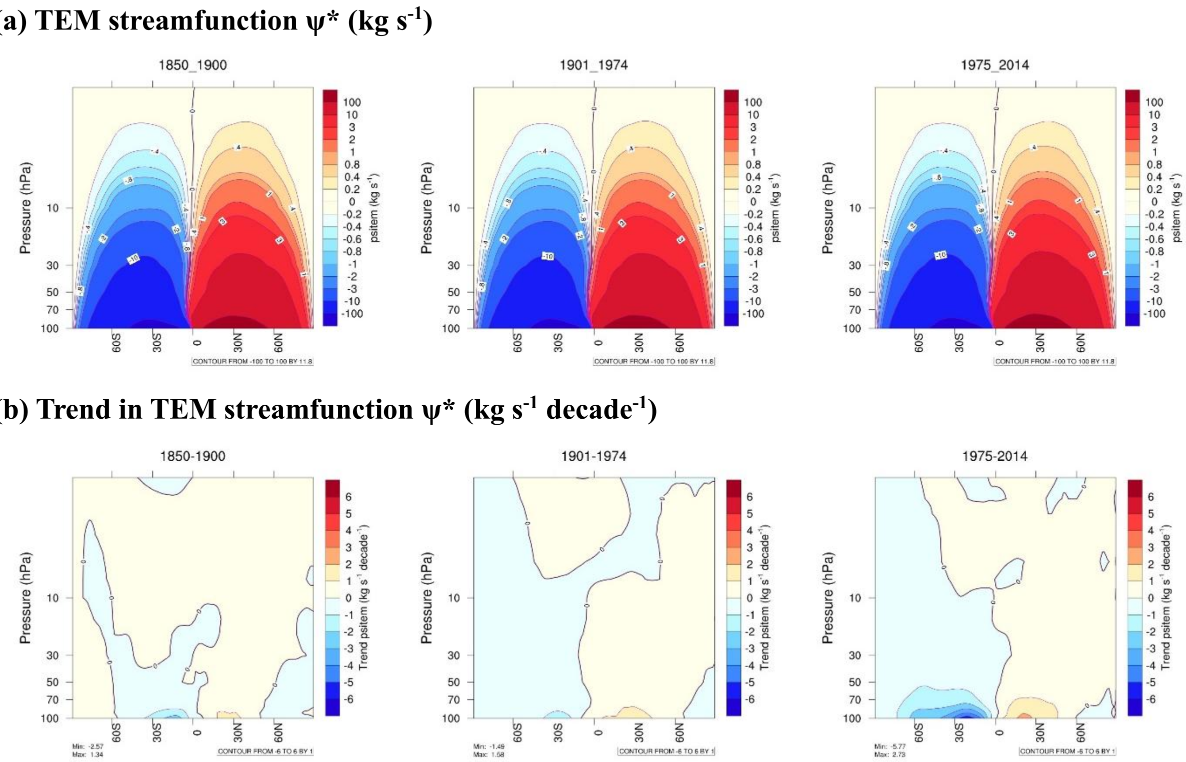

Figure 5. Latitude-pressure distribution of annually averaged (a) TEM residual streamfunction and (b) its trend per decade in pre-industry (1850-1900), past trend I (1901-1974) and past trend II (1975-2014) from the CMIP6 MIROC6 simulation driven by historical scenario.

3.3 Enhanced Wave-Driven Forcing of the Circulation

To investigate the mechanisms driving these changes, we analyze the zonal wind tendency components from CMIP6 1pctCO_2 simulations. The contribution from Eliassen–Palm (EP) flux divergence (utendepfd), which represents resolved wave forcing, shows a clear increase from the pre-industrial period to recent decades, particularly in the middle and upper stratosphere (80–20 hPa) (Fig. 6). The increasingly negative values of utendepfd indicate stronger momentum deposition due to enhanced planetary wave breaking.

This intensification of wave forcing is consistent with the expected response to greenhouse gas forcing, which increases tropospheric baroclinicity and enhances the generation and upward propagation of planetary waves (Castanheira et al., 2009). The resulting increase in momentum deposition drives stronger residual circulation and contributes directly to the acceleration of the BDC (Garcia and Randel, 2008). At the same time, a contrasting trend is observed in the uppermost stratosphere (10–1 hPa), where wave forcing weakens over time. This suggests a downward shift in the altitude of wave

https://doi.org/10.5194/egusphere-2026-4717
Preprint. Discussion started: 21 August 2026

breaking, with more momentum deposited in the lower stratosphere. Such a shift is consistent with changes in background wind structure, including a strengthened subtropical jet and modified wave propagation pathways (Oberländer-Hayn et al., 2016).

The redistribution of momentum deposition, rather than a uniform increase, therefore plays a key role in shaping the evolving structure of the BDC. Enhanced forcing in the lower and middle stratosphere supports stronger tropical upwelling and poleward transport, consistent with the observed reduction in AoA.

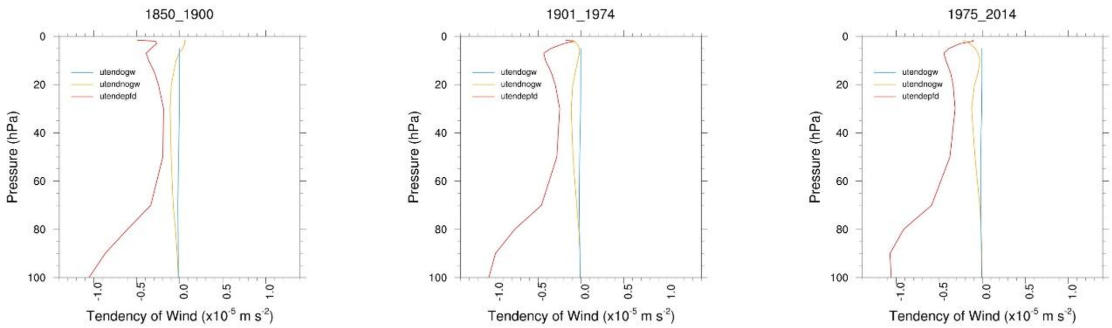

Figure 6. Vertical profile of wave forcing of the residual circulation driven by 1pctCO2 simulations during (a) pre-industrial (1850-1990), (b) past trend (1901-1974), and (c) recent trend (1975-2014). Red line represents total upwelling due to resolved waves computed from the Eliassen–Palm flux divergence (EPFD); yellow line represents total upwelling due to non-orographic gravity waves (NOGW); blue line represents total upwelling due to orographic gravity waves (OGW).

3.4 Observed Brewer–Dobson Transport from MLS H_2O Diagnostics

To complement the model-based circulation diagnostics, Aura MLS daily H_2O anomalies were analyzed across tropical, midlatitude, and polar latitude bands to investigate the observed propagation structure of large-scale Brewer–Dobson circulation (BDC) transport (Fig. 7). The anomaly evolution reveals coherent tropical-to-extratropical transport signatures throughout the lower and middle stratosphere, with particularly strong moistening signals emerging after the 2022 Hunga Tonga eruption. Positive H_2O anomalies first appear within the tropical lower stratosphere before progressively extending poleward and upward into the midlatitude and polar regions, especially within the Southern Hemisphere. This large-scale progression is consistent with residual-circulation-driven transport and provides a clear observational example of meridional tracer redistribution by the BDC.

https://doi.org/10.5194/egusphere-2026-4717
Preprint. Discussion started: 21 August 2026

To isolate intrinsic transport variability, lag-correlation diagnostics were calculated using the pre-eruption period (2004–2021), thereby excluding the large Hunga Tonga perturbation. Daily H_2O anomalies were first smoothed using a 31-point low-pass filter to suppress short-timescale variability while retaining large-scale transport evolution. The resulting lag-correlation structures reveal progressively longer transport timescales with increasing altitude and poleward distance from the tropics (Fig. 8a). The strongest lower-stratospheric relationship occurs within the 400–500 K layer, where tropical-to-midlatitude propagation peaks near 45–55 days. In contrast, tropical-to-polar propagation requires substantially longer timescales, reaching approximately 95–111 days within the 400–500 K layer and extending to ~224–362 days above 500 K. These increasingly delayed lag maxima indicate that tracer transport becomes progressively slower and more dynamically isolated away from the tropical lower stratosphere.

The lag-correlation diagnostics primarily characterize the temporal coherence and propagation structure of large-scale transport pathways, whereas the subsequent Flury-style framework quantifies the effective propagation speed associated with those pathways. Although both methods employ lag correlations, they diagnose complementary aspects of BDC transport behavior. The continuous lag-correlation framework identifies dynamically coherent propagation structures and characteristic transport delays, while the Flury-style analysis converts physically constrained lag relationships into effective tracer transport speeds.

Tracer propagation speeds derived from the MLS daily anomaly diagnostics reveal a pronounced vertical dependence in BDC transport efficiency (Table 5). Because broad hemispheric coherence and autocorrelation can generate unrealistically short lag maxima at daily resolution, physically constrained minimum lag thresholds were imposed prior to selecting final propagation timescales. Several lower-stratospheric pathways initially exhibited raw lag maxima near 1–16 days, particularly within the Northern Hemisphere lower stratosphere. These short-lag peaks were interpreted primarily as persistence-related covariance rather than dynamically realistic large-scale transport and were therefore excluded from the final propagation estimates. After applying the physical lag constraints, the fastest transport occurs within the 400–500 K layer, where tropical-to-extratropical propagation occurs over approximately 45–111 days, corresponding to effective tracer propagation speeds of ~60–74 km day^{-1}. Transport becomes substantially slower above 500 K. Within the 500–600 K layer, tropical-to-polar propagation requires approximately 265–362 days, with effective transport speeds reduced to ~18–37 km day^{-1}. Similarly, the 600–800 K layer exhibits slower and more variable propagation generally below ~30 km day^{-1}. Although all retained lag relationships remain statistically significant ($p < 0.05$), correlation strength generally decreases with increasing altitude and propagation distance, indicating progressively weaker dynamical coherence and stronger transport isolation within the middle stratosphere and polar regions.

To assess the sensitivity of the inferred transport timescales to temporal aggregation, an additional lag-correlation analysis using monthly averaged MLS H_2O anomalies was performed (Supplementary Material, Table S1). Although monthly

https://doi.org/10.5194/egusphere-2026-4717
Preprint. Discussion started: 21 August 2026

averaging discretizes the lag structure into broader temporal intervals, the monthly diagnostics reproduce the same overall vertical transport hierarchy identified in the daily analysis. Both frameworks consistently show faster tropical-to-extratropical propagation within the 400–500 K layer and substantially slower transport above 500 K, especially for tropical-to-polar pathways. The agreement between the daily and monthly analyses demonstrates that the inferred vertical structure of BDC transport efficiency is robust and not strongly dependent on the temporal resolution of the tracer diagnostics.

To evaluate whether the Flury-style propagation estimates depend on the selected minimum physical lag threshold, an additional daily sensitivity analysis was performed using alternative thresholds of 30–60 for tropical-to-midlatitude transport and 60–120 days for tropical-to-polar transport (Fig. 9). The results show that the inferred vertical hierarchy of tracer propagation is robust across all tested thresholds. The 500–600 K and 600–800 K layers exhibit minimal sensitivity, with normalized propagation speeds remaining close to unity relative to the default thresholds. In contrast, the 400–500 K layer shows greater sensitivity, particularly for tropical-to-midlatitude pathways, indicating that multiple physically plausible lag maxima exist within the lower stratosphere. Nevertheless, the main conclusion is unchanged: lower-stratospheric tracer propagation remains more responsive and dynamically active than transport above 500 K, while the middle-stratospheric layers remain comparatively stable and isolated. This confirms that the diagnosed vertical structure of BDC transport efficiency is not an artifact of the adopted 45-day and 90-day lag thresholds.

The MLS diagnostics therefore provide direct observational evidence that BDC transport efficiency is strongly altitude dependent, with the most efficient tracer redistribution occurring within the lower stratosphere. This vertical structure closely aligns with the CMIP6 dynamical diagnostics presented in Sections 3.1–3.3. In particular, the strongest tracer propagation occurs within the same altitude range where enhanced EP-flux divergence and strengthened wave-driven forcing are concentrated (80–20 hPa), supporting the interpretation that intensified lower-stratospheric wave forcing contributes directly to enhanced residual circulation transport. The MLS observations additionally provide an important observational constraint on the modeled AoA reductions. While the CMIP6 simulations indicate widespread decreases in stratospheric age of air under greenhouse forcing, the MLS tracer diagnostics demonstrate that these reductions are dynamically consistent with accelerated lower-stratospheric tracer redistribution rather than uniform transport acceleration throughout the entire stratosphere. Collectively, the combined AoA, TEM, EP-flux, and MLS diagnostics indicate that greenhouse-forced BDC changes are expressed primarily through enhanced lower-stratospheric transport efficiency and more rapid meridional redistribution, while transport within the middle stratosphere remains comparatively slower and more dynamically isolated.

https://doi.org/10.5194/egusphere-2026-4717
Preprint. Discussion started: 21 August 2026

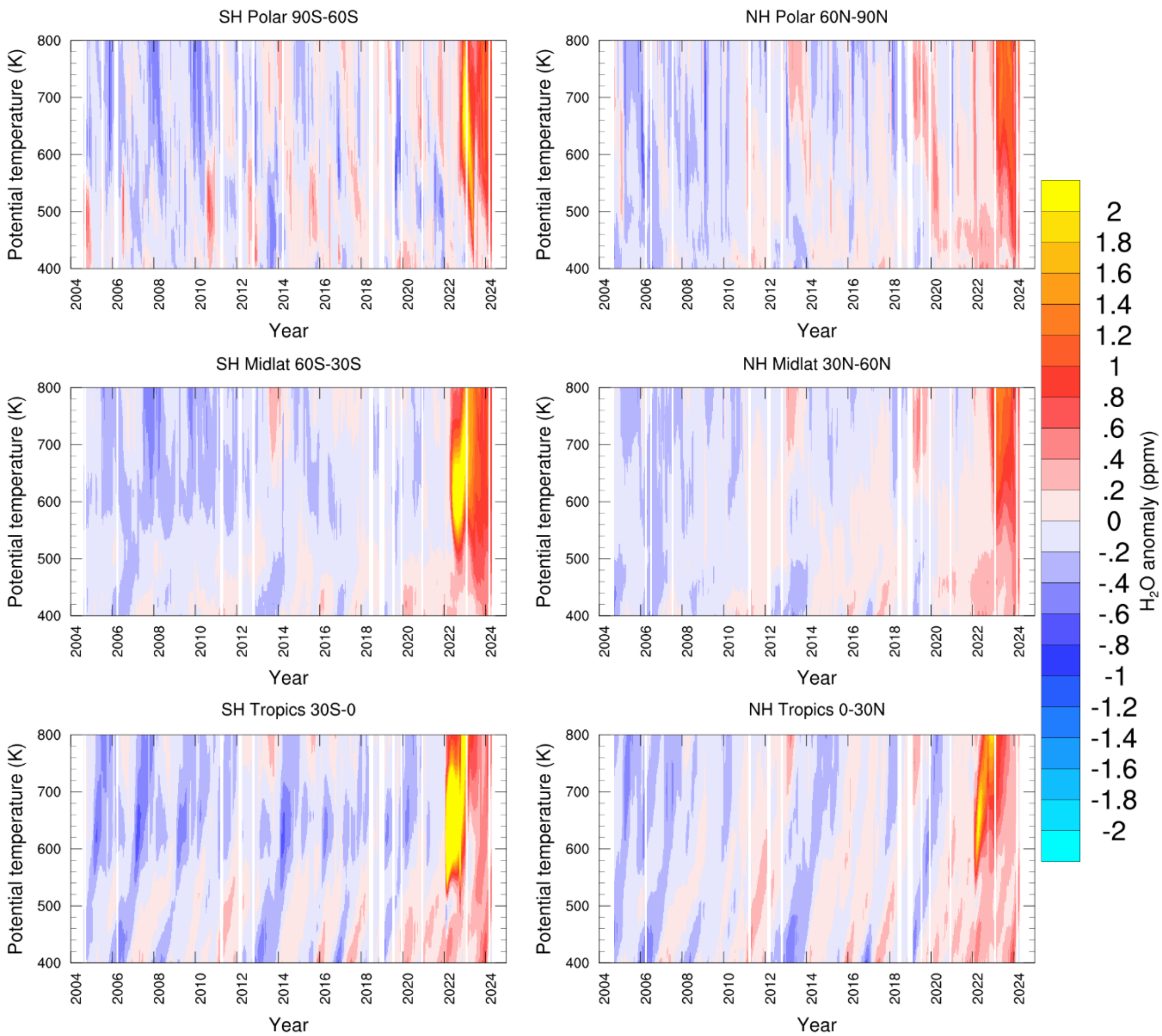

Figure 7. Time–potential temperature cross sections of Aura MLS H_2O anomalies (ppmv) averaged over six latitude bands from 2004–2024: SH polar (90°S–60°S), NH polar (60°N–90°N), SH midlatitudes (60°S–30°S), NH midlatitudes (30°N–60°N), SH tropics (30°S–0°), and NH tropics (0°–30°N). Positive anomalies after 2022 reveal enhanced stratospheric moistening associated with the Hunga Tonga eruption and subsequent meridional redistribution by the Brewer–Dobson circulation.

https://doi.org/10.5194/egusphere-2026-4717
Preprint. Discussion started: 21 August 2026

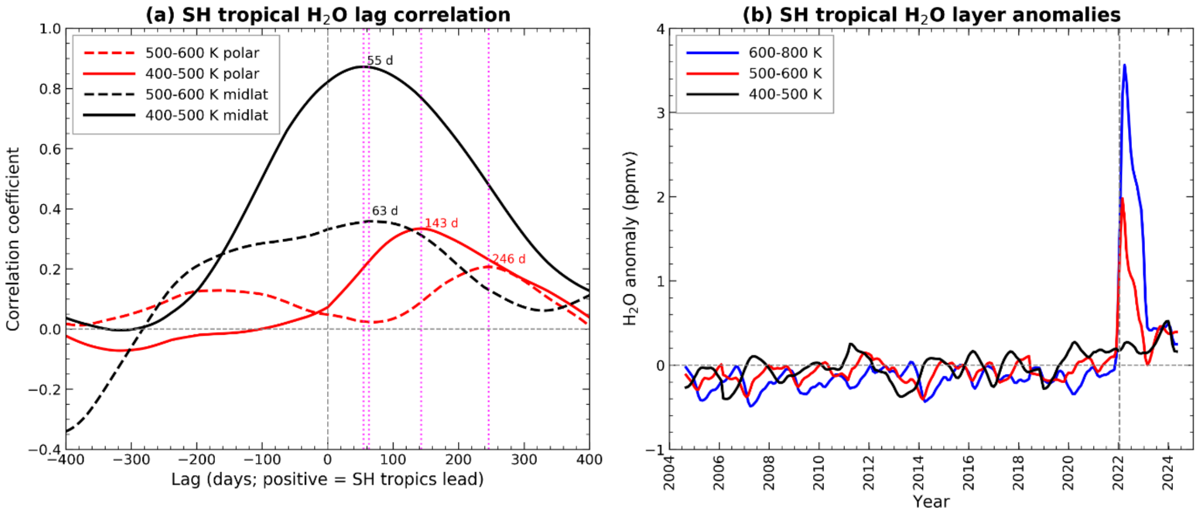

Figure 8. (a) Lag correlations between Southern Hemisphere tropical H_2O anomalies and corresponding midlatitude and polar anomalies for the 400–500 K and 500–600 K layers during the pre-eruption period (2004–
430 2021). Positive lag indicates the tropical anomalies lead extratropical variability. Vertical magenta dashed lines indicate peak lag correlations. (b) Time series of Southern Hemisphere tropical H_2O anomalies averaged over the 400–500 K, 500–600 K, and 600–800 K layers. Strong positive anomalies after 2022 reflect enhanced lower-stratospheric moistening associated with the Hunga Tonga eruption and subsequent transport through the Brewer–Dobson circulation.

https://doi.org/10.5194/egusphere-2026-4717
Preprint. Discussion started: 21 August 2026

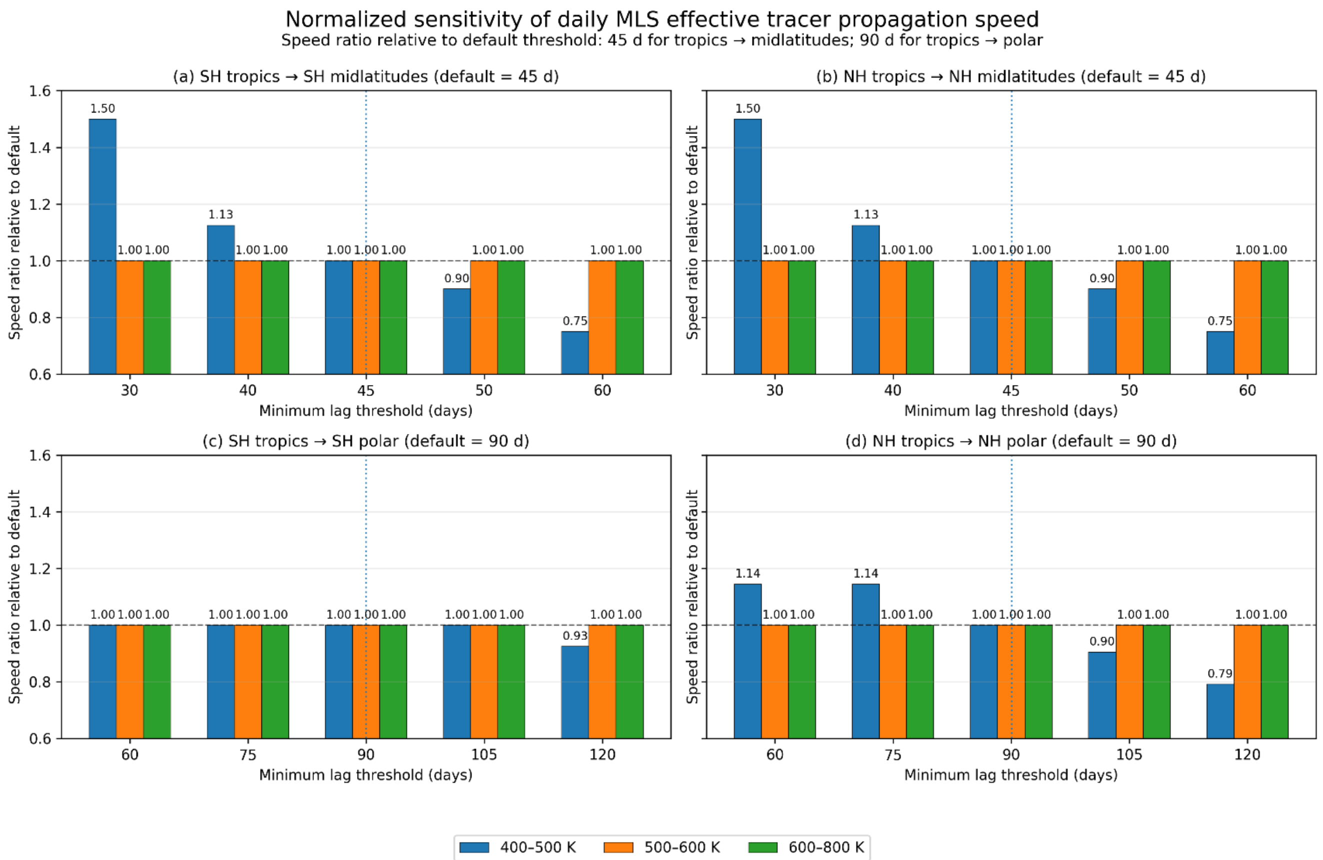

Figure 9. Sensitivity of normalized daily MLS effective tracer propagation speeds to the minimum physical lag threshold used in the Flury-style lag-correlation framework. Panels (a) and (b) show tropical-to-midlatitude transport using thresholds of 30–60 days, while panels (c) and (d) show tropical-to-polar transport using thresholds of 60–120 days. Propagation speeds are normalized relative to the default thresholds (45 and 90 days, respectively), indicated by the vertical dotted lines. The consistent vertical transport hierarchy across all tested thresholds demonstrates the robustness of the inferred transport structure.

https://doi.org/10.5194/egusphere-2026-4717
Preprint. Discussion started: 21 August 2026

Table 5. Effective tracer propagation timescales and transport speeds derived from Aura MLS H_2O daily anomaly lag-correlation diagnostics during the pre-eruption period (2004–2021). Final lag times were selected using physically constrained minimum thresholds of 45 days for tropical-to-midlatitude transport and 90 days for tropical-to-polar transport to minimize unrealistically short persistence-related covariance. Effective propagation speed represents great-circle meridional distance divided by the selected lag timescale.

Layer	Source → Target	Filtered lag (days)	rmax	p-value	Effective speed (km day^{-1})
400–500 K	SH tropics → SH midlatitudes	45	0.82	<0.001	74.1
400–500 K	SH tropics → SH polar	111	0.38	<0.001	60.1
400–500 K	NH tropics → NH midlatitudes	45	0.82	<0.001	74.1
400–500 K	NH tropics → NH polar	95	0.72	<0.001	70.2
500–600 K	SH tropics → SH midlatitudes	120	0.32	<0.001	27.8
500–600 K	SH tropics → SH polar	265	0.14	<0.001	25.2
500–600 K	NH tropics → NH midlatitudes	90	0.56	<0.001	37.1
500–600 K	NH tropics → NH polar	362	0.18	<0.001	18.4
600–800 K	SH tropics → SH midlatitudes	137	0.50	<0.001	24.3
600–800 K	SH tropics → SH polar	224	0.51	<0.001	29.8
600–800 K	NH tropics → NH midlatitudes	209	0.57	<0.001	16.0
600–800 K	NH tropics → NH polar	242	0.46	<0.001	27.6

4. Discussions & Conclusions

4.1 Wave–Mean Flow Interaction as the Primary Driver of Enhanced Transport Efficiency

The combined CMIP6 diagnostics indicate that greenhouse-gas forcing modifies Brewer–Dobson circulation (BDC) transport primarily through changes in wave–mean flow interaction rather than through major structural reorganization of the overturning circulation (Butchart, 2014; Garcia and Randel, 2008). The EP-flux diagnostics show enhanced wave-driven momentum deposition within the lower and middle stratosphere, particularly within the 80–20 hPa layer. This vertical region corresponds closely to the altitude range where the strongest lower-stratospheric tracer propagation is later identified from the MLS diagnostics. The increasingly negative EP-flux tendency indicates stronger planetary-wave momentum deposition, which is dynamically consistent with enhanced residual circulation transport under the transformed Eulerian mean framework (Mclandress and Shepherd, 2009).

Importantly, the enhanced wave forcing is vertically non-uniform. Momentum deposition strengthens primarily within the lower and middle stratosphere, while weaker responses occur in the uppermost stratosphere. This suggests that greenhouse forcing preferentially enhances transport within the shallow branch of the BDC rather than uniformly accelerating the entire overturning circulation (Baikhadzhaev et al., 2025). The TEM diagnostics further show that the turnaround latitude remains approximately stable near 30° in both hemispheres, indicating that the large-scale circulation geometry is broadly preserved. Therefore, the dominant response is not a major shift in circulation structure, but an increase in the efficiency of transport

https://doi.org/10.5194/egusphere-2026-4717
Preprint. Discussion started: 21 August 2026

within existing circulation pathways. Although residual streamfunction output is available only from MIROC6, this diagnostic provides qualitative support for the same interpretation. The streamfunction trends suggest enhanced poleward mass flux, particularly in the lower stratosphere, but they are interpreted here as supporting evidence rather than as an independent multi-model constraint. Taken together, the EP-flux and TEM diagnostics provide a physically consistent mechanism linking greenhouse forcing to enhanced lower-stratospheric transport efficiency.

4.2 Integrated Model and Observational Evidence for Enhanced Lower-Stratospheric Transport

The main contribution of this study is the integration of complementary diagnostics that describe different components of the BDC transport system. Rather than relying on a single metric, enhanced transport efficiency is inferred from the consistency among AoA, TEM, EP-flux, and MLS tracer diagnostics (Butchart, 2014). The AoA simulations provide the strongest model-based evidence for accelerated large-scale transport. Across the CMIP6 ensemble, AoA decreases from the pre-industrial period to the recent historical period and continues to decrease under SSP370 projections (Garcia and Randel, 2008). The disappearance or weakening of high-AoA regions, particularly values exceeding approximately 6 years in the earlier historical periods, indicates progressively younger stratospheric air and shorter transport timescales. In the far-future SSP370 period, the upper stratosphere is dominated by younger air masses below approximately 4.4 years across seasons, suggesting continued acceleration of large-scale transport into the late 21st century.

The MLS diagnostics provide an independent observational constraint on this model-based interpretation. During the pre-eruption period from 2004 to 2021, lag-correlation analysis of daily MLS H_2O anomalies reveals coherent tropical-to-extratropical propagation pathways. The strongest lower-stratospheric relationships occur within the 400–500 K layer, where tropical-to-midlatitude propagation peaks near 45–55 days. Tropical-to-polar propagation requires longer timescales, approximately 95–111 days within the same 400–500 K layer. Above 500 K, the propagation timescales become substantially longer, reaching approximately 224–362 days for tropical-to-polar pathways. This vertical progression demonstrates that tracer redistribution becomes slower and more dynamically isolated with increasing altitude and meridional distance from the tropics. The Flury-style tracer propagation analysis further quantifies this vertical dependence. Effective tracer propagation speeds are highest within the 400–500 K layer, reaching approximately 60–74 km day^{-1} for tropical-to-extratropical transport. In contrast, speeds decrease substantially above 500 K. Within the 500–600 K layer, tropical-to-polar propagation speeds are reduced to approximately 18–37 km day^{-1}, while the 600–800 K layer generally shows slower and more variable propagation, mostly below approximately 30 km day^{-1}. Although the retained lag relationships are statistically significant, the correlation strength weakens with altitude and propagation distance, indicating reduced dynamical coherence in the middle stratosphere and polar regions.

These observational results are dynamically consistent with the CMIP6 diagnostics. The fastest tracer propagation occurs within the same lower-stratospheric region where enhanced EP-flux divergence and stronger wave-driven forcing are

https://doi.org/10.5194/egusphere-2026-4717
Preprint. Discussion started: 21 August 2026

concentrated. Therefore, the MLS tracer diagnostics support the interpretation that CMIP6-simulated AoA reductions are not simply indicative of uniform transport acceleration throughout the stratosphere but are instead most consistent with enhanced lower-stratospheric tracer redistribution (Poshyvailo-Strube et al., 2022). Monthly averaged MLS diagnostics reproduce the same vertical hierarchy, further indicating that the inferred structure of faster lower-stratospheric and slower middle-stratospheric transport is not strongly dependent on the temporal resolution of the tracer analysis. It is important, however, that the MLS lag-correlation results are interpreted as effective tracer-propagation diagnostics rather than as direct measurements of advective velocity. Tracer propagation reflects the combined effects of residual advection, wave-driven mixing, persistence, and recirculation (Šácha et al., 2023). Nevertheless, the agreement among AoA, TEM, EP-flux, and MLS diagnostics provides robust evidence that greenhouse-forced BDC changes are expressed primarily through enhanced lower-stratospheric transport efficiency and more rapid meridional redistribution, while the middle stratosphere remains comparatively slower and more dynamically isolated.

4.3 Implications for Stratospheric Composition and Climate Coupling

The results suggest that future BDC changes should be interpreted not only in terms of circulation strength but also in terms of transport efficiency. Traditional diagnostics such as TEM vertical velocity and residual streamfunction describe the overturning circulation, while AoA and tracer propagation describe the integrated effect of circulation and mixing on air-mass and tracer redistribution. The distinction is important because enhanced transport efficiency can occur even when the large-scale circulation geometry remains relatively stable (Gerber, 2012). The preferential enhancement of lower-stratospheric transport has important implications for atmospheric composition. Faster transport within the shallow branch of the BDC implies shorter residence times for long-lived tracers and more rapid redistribution of chemically and radiatively active species such as ozone and water vapor (Hufnagl et al., 2023). Enhanced tropical upwelling may increase the injection of tropospheric constituents into the lower stratosphere, while stronger meridional redistribution may transport these constituents more efficiently toward higher latitudes(Poshyvailo-Strube et al., 2022). However, the slower propagation above 500 K indicates that the middle stratosphere and polar regions retain stronger dynamical isolation. Future changes in stratospheric composition may therefore be concentrated primarily in the lower stratosphere rather than being uniformly distributed throughout the entire stratosphere.

The 2022 Hunga Tonga moistening event further illustrates the value of episodic tracer perturbations for diagnosing large-scale transport. The observed progression of positive H_2O anomalies from the tropical lower stratosphere into extratropical regions is consistent with BDC-mediated redistribution (Chang et al., 2025) and provides a real-world example of the transport pathways inferred from the pre-eruption lag analysis. Although the main transport diagnostics were calculated using the pre-eruption period to avoid contamination by this exceptional perturbation, the post-eruption anomaly evolution visually reinforces the interpretation that the lower stratosphere provides an efficient pathway for large-scale tracer redistribution. More broadly, this study demonstrates the value of combining model simulations with observation-based

https://doi.org/10.5194/egusphere-2026-4717
Preprint. Discussion started: 21 August 2026

tracer propagation diagnostics. By linking dynamical forcing, residual circulation response, integrated transport timescales, and observed tracer redistribution, the framework provides a physically consistent approach for evaluating greenhouse-forced changes in stratospheric transport.

4.4 Limitations and Future Perspectives

Several limitations should be considered when interpreting these results. First, the residual streamfunction analysis is based primarily on MIROC6, limiting direct assessment of inter-model variability in overturning structure across the broader CMIP6 ensemble. The streamfunction results are therefore used as qualitative supporting evidence rather than as a multi-model constraint. Future studies should incorporate additional models with available streamfunction diagnostics to better assess the robustness of circulation-geometry changes.

Second, the MLS lag-correlation framework diagnoses effective tracer propagation rather than purely advective velocity. Daily anomaly analyses preserve the temporal evolution of large-scale transport pathways but remain susceptible to persistence-related covariance and short-lag hemispheric coherence. Physically constrained minimum lag thresholds of 45 days for tropical-to-midlatitude transport and 90 days for tropical-to-polar transport were therefore adopted to reduce unrealistically short lag maxima. A sensitivity analysis using alternative threshold values demonstrates that the inferred vertical transport hierarchy remains unchanged, indicating that the enhanced lower-stratospheric transport identified in this study is not an artifact of the selected lag thresholds. Interestingly, the 400–500 K layer exhibits greater sensitivity to threshold selection than the overlying layers, suggesting the presence of multiple physically plausible propagation timescales, whereas transport above 500 K is characterized by a more stable dominant timescale. Future trajectory-based and tracer transport studies are required to determine whether this behaviour reflects the combined influences of residual circulation, wave-driven mixing, or other transport processes.

Third, the present analysis does not fully separate the relative contributions of residual advection, mixing, and recirculation. Additional tracer-based diagnostics, chemically active species, and Lagrangian transport calculations would help clarify the physical mechanisms underlying the effective tracer propagation speeds inferred from MLS H_2O.

Finally, this study focuses primarily on zonal-mean large-scale circulation variability. Future work should investigate how greenhouse-forced changes in BDC transport efficiency interact with regional dynamical processes, including the Quasi-Biennial Oscillation, sudden stratospheric warmings, ENSO, and other modes of interannual variability. Extending this observationally constrained framework to additional long-lived tracers would further improve understanding of how enhanced lower-stratospheric transport influences ozone recovery, stratospheric water vapor, and climate feedbacks.

https://doi.org/10.5194/egusphere-2026-4717
Preprint. Discussion started: 21 August 2026

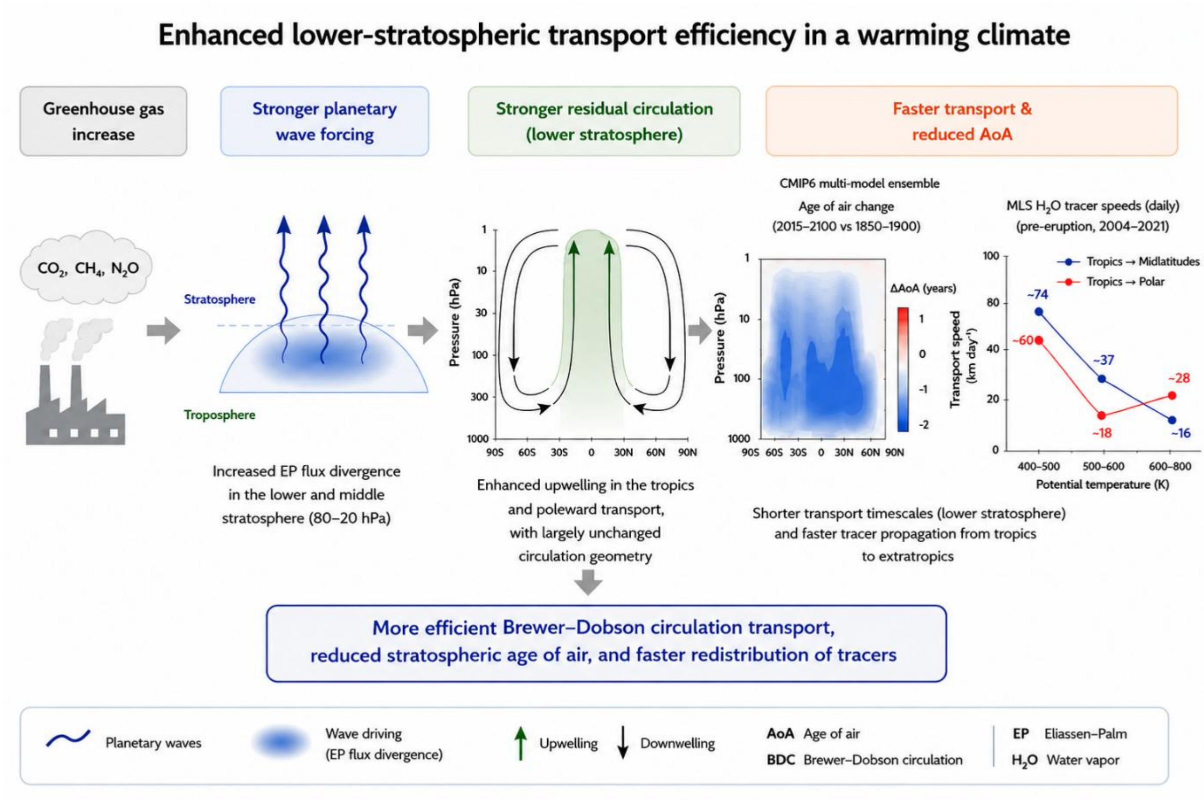

Figure 10. Conceptual schematic summarizing the proposed mechanism linking greenhouse-gas forcing to enhanced lower-stratospheric Brewer–Dobson circulation (BDC) transport efficiency. Increased greenhouse-gas concentrations enhance planetary wave activity and Eliassen–Palm (EP) flux divergence within the lower and middle stratosphere (approximately 80–20 hPa), leading to stronger residual circulation transport and more efficient tropical upwelling and poleward redistribution. The enhanced lower-stratospheric transport is associated with shorter stratospheric age-of-air (AoA) timescales and faster propagation of MLS H_2O tracers from the tropics toward the extratropics. The combined CMIP6 and observational diagnostics indicate that greenhouse-forced BDC changes are expressed primarily through enhanced lower-stratospheric transport efficiency and tracer redistribution rather than major structural changes in the overall circulation geometry.

Code and data availability

The CMIP6 simulations analyzed in this study were obtained from the Earth System Grid Federation (ESGF) data archive. Aura Microwave Limb Sounder (MLS) Level-3 zonal mean H_2O observations were obtained from the NASA Goddard Earth

https://doi.org/10.5194/egusphere-2026-4717
Preprint. Discussion started: 21 August 2026

Sciences Data and Information Services Center (GES DISC). All data processing and analysis were performed using Python and NCAR Command Language (NCL) scripts developed by the authors, which are available upon request.

Supplement link

The link to the supplement will be included by Copernicus, if applicable.

Author contributions

Jackson Hian-Wui Chang conceived the study, performed the analysis, interpreted the results, and wrote the manuscript. Ahmad Fairudz bin Jamaluddin, Sharifah Faridah binti Syed Mahbar performed data curation and data analysis. Yong Jie Wong, Maggie Chel-Gee Ooi, Juneng Liew, Fuei Pien Chee, Jedol Dayou, and Justin Sentian contributed to the interpretation of the results and reviewed the manuscript. Raul R. Cordero and Neng-Huei Lin supervised the research, contributed to the interpretation of the results, and reviewed the manuscript. All authors approved the final manuscript.

Competing interests

The authors declare that they have no conflict of interest.

Disclaimer

Copernicus Publications remains neutral with regard to jurisdictional claims made in the text, published maps, institutional affiliations, or any other geographical representation in this paper. While Copernicus Publications makes every effort to include appropriate place names, the final responsibility lies with the authors. Views expressed in the text are those of the authors and do not necessarily reflect the views of the publisher.

Acknowledgements

The authors acknowledge the World Climate Research Programme (WCRP), the Coupled Model Intercomparison Project Phase 6 (CMIP6), and the participating modeling groups for producing and making available the CMIP6 simulations used in this study. The authors also acknowledge the Earth System Grid Federation (ESGF) for providing access to the CMIP6 archive. Aura Microwave Limb Sounder (MLS) observations were obtained from the NASA Goddard Earth Sciences Data and Information Services Center (GES DISC). The authors thank the Aura MLS science team for providing the Level-3 H_2O datasets used in this analysis.

https://doi.org/10.5194/egusphere-2026-4717
Preprint. Discussion started: 21 August 2026

Financial support

This study was supported by research funding from Yayasan Penyelidikan Antartika Sultan Mizam (YPASM) 2026 and internal research funding from Universiti Malaysia Sabah

Review statement

The review statement will be added by Copernicus Publications listing the handling editor as well as all contributing referees according to their status anonymous or identified.

References

Baikhadzhaev, R., Ploeger, F., Preusse, P., Ern, M., and Birner, T.: A dynamics-based separation of deep and shallow stratospheric circulation branches, Atmos. Chem. Phys., 25, 12753–12777, https://doi.org/10.5194/acp-25-12753-2025, 2025.

Bunzel, F. and Schmidt, H.: The Brewer–Dobson Circulation in a Changing Climate: Impact of the Model Configuration, Journal of the Atmospheric Sciences, 70, 1437–1455, https://doi.org/10.1175/jas-d-12-0215.1, 2013.

Butchart, N.: The Brewer-Dobson circulation, Rev. Geophys., 52, 157–184, https://doi.org/10.1002/2013rg000448, 2014.

Carr, E. S., Harwood, R. S., Mote, P. W., Peckham, G. E., Suttie, R. A., Lahoz, W. A., O'Neill, A., Froidevaux, L., Jarnot, R. F., Read, W. G., Waters, J. W., and Swinbank, R.: Tropical stratospheric water vapor measured by the Microwave Limb Sounder (MLS), Geophysical Research Letters, 22, 691–694, https://doi.org/10.1029/95gl00626, 1995.

Castanheira, J. M., Añel, J. A., Marques, C. A. F., Antuña, J. C., Liberato, M. L. R., De La Torre, L., and Gimeno, L.: Increase of upper troposphere/lower stratosphere wave baroclinicity during the second half of the 20th century, Atmos. Chem. Phys., 9, 9143–9153, https://doi.org/10.5194/acp-9-9143-2009, 2009.

Chang, J. H.-W., Pien, C. F., Sentian, J., Cordero, R. R., Ooi, M. C.-G., and Wong, Y. J.: Evidence of localized H_2O increases and O_3 recovery in the Antarctic lower stratospheric vortex: MLS observations and BDC variability during late winter to spring, Atmospheric Research, 328, 108428, https://doi.org/10.1016/j.atmosres.2025.108428, 2025.

Clark, H. L., Harwood, R. S., Mote, P. W., and Read, W. G.: Variability of water vapor in the tropical upper troposphere as measured by the Microwave Limb Sounder on UARS, J. Geophys. Res., 103, 31695–31707, https://doi.org/10.1029/98jd02702, 1998.

Coy, L., Newman, P. A., Wargan, K., Partyka, G., Strahan, S. E., and Pawson, S.: Stratospheric Circulation Changes Associated With the Hunga Tonga-Hunga Ha'apai Eruption, Geophysical Research Letters, 49, https://doi.org/10.1029/2022gl100982, 2022.

Flury, T., Wu, D. L., and Read, W. G.: Variability in the speed of the Brewer–Dobson circulation as observed by Aura/MLS, Atmos. Chem. Phys., 13, 4563–4575, https://doi.org/10.5194/acp-13-4563-2013, 2013.

Garcia, R. R. and Randel, W. J.: Acceleration of the Brewer–Dobson Circulation due to Increases in Greenhouse Gases, Journal of the Atmospheric Sciences, 65, 2731–2739, https://doi.org/10.1175/2008jas2712.1, 2008.

Gerber, E. P.: Stratospheric versus Tropospheric Control of the Strength and Structure of the Brewer–Dobson Circulation, Journal of the Atmospheric Sciences, 69, 2857–2877, https://doi.org/10.1175/jas-d-11-0341.1, 2012.

Gerber, E. P. and Manzini, E.: The Dynamics and Variability Model Intercomparison Project (DynVarMIP) for CMIP6: assessing the stratosphere–troposphere system, Geosci. Model Dev., 9, 3413–3425, https://doi.org/10.5194/gmd-9-3413-2016, 2016.

Hall, T. M. and Waugh, D. W.: Timescales for the stratospheric circulation derived from tracers, J. Geophys. Res., 102, 8991–9001, https://doi.org/10.1029/96jd03713, 1997.

Hoor, P., Wernli, H., Hegglin, M. I., and Bönisch, H.: Transport timescales and tracer properties in the extratropical UTLS, Atmos. Chem. Phys., 10, 7929–7944, https://doi.org/10.5194/acp-10-7929-2010, 2010.

Hufnagl, L., Eichinger, R., Garny, H., Birner, T., Kuchař, A., Jöckel, P., and Graf, P.: Stratospheric Ozone Changes Damp the CO2-Induced Acceleration of the Brewer–Dobson Circulation, Journal of Climate, 36, 3305–3320, https://doi.org/10.1175/jcli-d-22-0512.1, 2023.

Kawatani, Y., Lee, J. N., and Hamilton, K.: Interannual Variations of Stratospheric Water Vapor in MLS Observations and Climate Model Simulations, Journal of the Atmospheric Sciences, 71, 4072–4085, https://doi.org/10.1175/jas-d-14-0164.1, 2014.

Mclandress, C. and Shepherd, T. G.: Simulated Anthropogenic Changes in the Brewer–Dobson Circulation, Including Its Extension to High Latitudes, Journal of Climate, 22, 1516–1540, https://doi.org/10.1175/2008jcli2679.1, 2009.

Oberländer-Hayn, S., Gerber, E. P., Abalichin, J., Akiyoshi, H., Kerschbaumer, A., Kubin, A., Kunze, M., Langematz, U., Meul, S., Michou, M., Morgenstern, O., and Oman, L. D.: Is the Brewer-Dobson circulation increasing or moving upward?, Geophysical Research Letters, 43, 1772–1779, https://doi.org/10.1002/2015gl067545, 2016.

Poshyvailo-Strube, L., Müller, R., Fueglistaler, S., Hegglin, M. I., Laube, J. C., Volk, C. M., and Ploeger, F.: How can Brewer–Dobson circulation trends be estimated from changes in stratospheric water vapour and methane?, Atmos. Chem. Phys., 22, 9895–9914, https://doi.org/10.5194/acp-22-9895-2022, 2022.

Randel, W. J., Podglajen, A., and Wu, F.: Stratospheric Transit Time Distributions Derived From Satellite Water Vapor Measurements, JGR Atmospheres, 129, https://doi.org/10.1029/2024jd041595, 2024.

Šácha, P., Zajíček, R., Kuchar, A., Eichinger, R., Pisoft, P., and Rieder, H. E.: Unravelling the kinematics of the Brewer-Dobson circulation change, https://doi.org/10.22541/essoar.169230312.27488559/v1, 17 August 2023.

Šácha, P., Zajíček, R., Kuchař, A., Eichinger, R., Pišoft, P., and Rieder, H. E.: Disentangling the Advective Brewer-Dobson Circulation Change, Geophysical Research Letters, 51, https://doi.org/10.1029/2023gl105919, 2024.

Salby, M. L. and Callaghan, P. F.: Influence of the Brewer-Dobson circulation on stratosphere-troposphere exchange, J. Geophys. Res., 111, https://doi.org/10.1029/2006jd007051, 2006.

Smith, C. J. and Forster, P. M.: Suppressed Late-20th Century Warming in CMIP6 Models Explained by Forcing and Feedbacks, Geophysical Research Letters, 48, https://doi.org/10.1029/2021gl094948, 2021.

Tweedy, O. V., Waugh, D. W., Stolarski, R. S., Oman, L. D., Randel, W. J., and Abalos, M.: Hemispheric differences in the

https://doi.org/10.5194/egusphere-2026-4717
Preprint. Discussion started: 21 August 2026

annual cycle of tropical lower stratosphere transport and tracers, JGR Atmospheres, 122, 7183–7199, https://doi.org/10.1002/2017jd026482, 2017.

Yu, W., Garcia, R., Yue, J., Smith, A., Wang, X., Randel, W., Qiao, Z., Zhu, Y., Harvey, V. L., Tilmes, S., and Mlynczak, M.: Mesospheric Temperature and Circulation Response to the Hunga Tonga-Hunga-Ha'apai Volcanic Eruption, JGR Atmospheres, 128, https://doi.org/10.1029/2023jd039636, 2023.

Zajíček, R., Šácha, P., Pišoft, P., and Mikšovský, J.: Advective transport between the stratosphere and mesosphere, https://doi.org/10.5194/egusphere-egu24-21525, 2024.

Zanis, P., Akritidis, D., Georgoulias, A. K., Allen, R. J., Bauer, S. E., Boucher, O., Cole, J., Johnson, B., Deushi, M., Michou, M., Mulcahy, J., Nabat, P., Olivié, D., Oshima, N., Sima, A., Schulz, M., Takemura, T., and Tsigaridis, K.: Fast responses on pre-industrial climate from present-day aerosols in a CMIP6 multi-model study, Atmos. Chem. Phys., 20, 8381–8404, https://doi.org/10.5194/acp-20-8381-2020, 2020.